Fuel 266 (2020) 117077

Contents lists available at ScienceDirect

Fuel

journal homepage: www.elsevier.com/locate/fuel

Full Length Article

Autoignition and detonation characteristics of *n*-heptane/air mixture with water droplets

Yijie Zhuang[a], Qiang Li[a], Peng Dai[b,*], Huangwei Zhang[a,*]

[a] Department of Mechanical Engineering, National University of Singapore, 9 Engineering Drive 1, Singapore 117576, Singapore
[b] Department of Mechanics and Aerospace Engineering, Southern University of Science and Technology, Shenzhen 518055, China

ARTICLE INFO

Keywords:
Autoignition
Detonation development
n-heptane/air
Water droplet evaporation
Thermal inhomogeneity

ABSTRACT

The present study addresses the autoignition and detonation characteristics of *n*-heptane/air mixture with water droplets in a confined one-dimensional reactor. A Eulerian-Eulerian formulation for gas and liquid phases is employed to simulate multi-component, fully compressible and reactive multi-phase flows. The parametric investigations covering a range of droplet diameters and number densities are conducted to understand the reaction front development in gas phase and droplet evaporation characteristics under different gaseous combustion conditions. Four modes of autoignition behaviours in the reactor are identified and they are found to greatly depend on both droplet diameter and number density. At a relatively small droplet diameter and/or number density, detonation is initiated by hot spot but no autoignition occurs at the right boundary. When both or either of them increase, autoignition occurs at the right boundary and the reaction front may further evolve into detonative or deflagrative waves. This is because the temperature inhomogeneity in that region is considerably enhanced. Furthermore, droplet diameter and number density are used to quantify the different modes of autoignition and detonation development. For the droplet evaporation dynamics during the reactive front development process, various mechanisms are observed, related to the different effects dominated by the velocity difference between two phases (characterized by the droplet Reynolds number), high local gas pressure and also the droplet temperature. This results in non-monotonic spatial distributions of droplet evaporation rate in the reactor, e.g. *M*-shaped in the detonated or shocked regions.

1. Introduction

Recently downsizing of Spark Ignition Engines (SIE's) with turbocharging technology has become increasingly attractive [1]. However, knock is still a severe constraint of SIE's applying high compression ratio. Generally, knock in SIEs is caused by end-gas autoignition [2] and detonation resulting from coupling of chemical reaction and pressure wave plays an important role in super-knock [3,4]. On the other hand, most realistic energy conversion devices operate as multi-phase combustion systems. Furthermore, water injection, with an effective cooling effect for combustion process in different types of engines, has attracted extensive attentions in recent years due to the potential knock mitigation and NO_x reduction [5]. For these scenarios, different aspects of these or related problems are investigated during the last decades. Even so, there still lacks a comprehensive understanding of the physio-chemical processes in autoignition modes and detonation interactions with evaporating droplets.

There are extensive studies on autoignitive reaction front propagation since it is fundamentally related to engine knock phenomenon. In the pioneering work by Zel'dovich [6], it was proposed that different autoignition modes are caused by non-uniform reactivity. The theory was confirmed and further extended by theoretical analysis [7] and by simulations considering detailed chemical mechanisms [8–15]. Among them, Bradley and his co-workers [9–11] introduced an operational peninsula (normalized temperature gradient, ξ, versus ratio of acoustic time to excitation time, ε) for detonation development, which can be used to predict engine knock. Dai et al. [12–14] performed one-dimensional (1D) simulations to investigate detonation development regimes for *n*-heptane with low-temperature chemistry and Negative Temperature Coefficient (NTC) characteristics. They found that the reaction-pressure wave interactions become much more complicated in the presence of low-temperature chemistry and that a cold spot can also

* Corresponding authors at: Department of Mechanical Engineering, Faculty of Engineering, National University of Singapore, 9 Engineering Drive 1, Singapore 117576, Singapore (H. Zhang); Department of Mechanics and Aerospace Engineering, Southern University of Science and Technology, Shenzhen 518055, China (P. Dai).
E-mail addresses: daip@sustech.edu.cn (P. Dai), huangwei.zhang@nus.edu.sg (H. Zhang).

https://doi.org/10.1016/j.fuel.2020.117077
Received 17 September 2019; Received in revised form 11 December 2019; Accepted 10 January 2020
Available online 24 January 2020
0016-2361/

Nomenclature

A	surface area
B_M	Spalding mass transfer number
B_T	Spalding heat transfer number
C_p	specific heat
C_d	drag coefficient
d	droplet diameter
$D_{water,m}$	binary diffusion coefficient of water vapour in the gas-phase mixture
E	total energy
F_s	drag force
k_g	gas thermal diffusivity
Le	Lewis number
L_v	latent heat
M	mean molecular weight
$\dot{m}$	evaporation rate
m	mass
N	number density
n	number of species
Nu	Nusselt number
P	pressure
q	heat flux
R	universal gas constant
Re	Reynolds number
$\widetilde{Sh}$	modified Sherwood number
S	evaporation related source term
Sc	Schmidt number
t, x	temporal and spatial coordinates
T	temperature
U	velocity vector
u	flow velocity
$V^{'}$	diffusion velocity
X	mole fraction
Y	mass fraction

Greek letters

ρ	density
ω	production rate
μ	dynamic viscosity
τ_r	droplet momentum relaxation time
τ	viscous stress

Subscripts

v	momentum
d	droplet
e	energy
k	species k
m	species mass fraction
ref	reference value
0	initial

lead to detonation development when the initial temperature is within NTC regime. Recently, Dai. et al. [15] extended their work to autoignition and detonation development induced by a hot spot in fuel-lean and carbon dioxide diluted *n*-heptane/air mixtures. Besides, Yu et al. [16] performed a 1D simulation to study the end-gas autoignition and detonation development in a closed chamber, and identified three modes of end-gas combustion depending on the chamber length as well as the initial temperature and pressure: normal flame propagation without autoignition, autoignition without detonation, and detonation.

It is well established that the non-uniform thermodynamic state in an end-gas region is mainly perturbed by small scale phenomena such as pressure wave disturbance [17–19], turbulence [20], or thermal inhomogeneities [21–24]. Pan et al. [20] carried out an LES (Large Eddy Simulation) work to explore autoignition induced abnormal combustion based on a downsized SIE. Wei et al. [25] carried out experiments to investigate the relationship of turbulent flame, shock wave and autoignition in a confined chamber with a perforated plate. They experimentally observed three combustion modes, including normal combustion, oscillating combustion and end-gas autoignition. Recently, Terashima et al. [26–28] presented a series of work to reveal the mechanisms for the hot-spot formation and pressure wave development associated with end-gas autoignition during knocking combustion in *n*-heptane/air mixture. However, most of the previous studies on autoignition induced by non-uniform reactivity (e.g. hot spot) were only focused on purely gaseous mixtures. Very few studies have been carried out to understand the effects of gas-liquid droplet interaction on autoignition and knocking formation. However, the droplet evaporation may cause thermal and compositional stratification that triggers different autoignition modes.

A number of experimental [29–32] and computational [33–37] studies on two-phase shock/detonation have investigated either the phase change in the relaxation zone behind a pressure wave or the wave attenuation due to the gas-droplet interaction. Smirnov et al. [30] carried out investigations on detonation onset in pulverized fuel–air mixtures and found that the mixture polydispersity and non-uniformity of droplet spatial distribution strongly affect spray combustion and detonation initiation. Particularly, water mist has wide application in preventing and reducing gas explosion hazard [38,39], due to its easy availability and nontoxicity. Niedzielska et al. [32] conducted experiments to investigate the influence of water droplets on propagating detonations, and found that droplets with critical diameter (say 215 μm) can quench the detonation temporarily but the flow rapidly accelerates back to the initial detonation speed. Yeom et al. [35] elaborated how shock dissipation and pressure distribution are affected by droplet size and droplet volume fraction. Schwer et al. [36] suggested that momentum extraction plays a dominant role in mitigating the leading shock wave. Recently, Watanabe et al. [37] conducted a 2D numerical simulation to clarify the propagation behavior of gaseous detonation in a water spray and its structure. They found that adding water droplets changes the cellular pattern and the detonation flow field, and evaporation occurs primarily at 10 mm behind the shock wave.

Nevertheless, relatively less work has been published regarding autoignition and subsequent evolution of reaction front in two-phase mixtures. The influences of temperature, pressure, and droplet size on autoignition of liquid fuel sprays were discussed by Aggarwal [40]. Bouali et al. [41] numerically investigated the influence of liquid fuel presence on the autoignition of *n*-heptane/air mixtures over a wide range of conditions encountered in internal combustion engines. They pointed out that the spray properties (e.g. mass of droplets, droplet number density) play an important role in the evolution of the autoignition delay curve. Moreover, Wang et al. [42] reviewed knocking combustion in SIE's and it was commented that increased water content can suppress the autoignition of the end gas and therefore sometimes water mists or vapour are adopted as a knocking suppressant. Harrington [43] also investigated the influences of water addition to the injected fuels on NO_x emissions and knocking tendency of the engines. Hoppe et al. [44] explored the potential of water injection to reduce knocking phenomenon and improve overall combustion efficiency in direct injection gasoline engines. However, understanding of the physiochemical processes in autoignition modes and detonation interactions with evaporating droplets remains to be improved.

Therefore, the objective of the present work is to analyze how the water droplet evaporation influences autoignition and detonation development in *n*-heptane/air mixture. The emphasis will be laid on the underlying mechanisms responsible for the two-phase detonation system, and their effects on the autoignition and detonation development modes, as well as the water droplet evaporation in the detonated gas. The rest of the paper is structured as below. Models and methodology are presented in Section 2. Results from the numerical simulations will be discussed in detail in Section 3. Section 4 closes the paper with the main conclusions.

2. Models and methodology

2.1. Numerical method

The Eulerian-Eulerian approach is applied to simulate the transient autoignition process initiated by a hot spot in stoichiometric *n*-heptane/air mixture as well as its interaction with a mono-dispersed water mist in a 1D closed, planar reactor. An in-house solver, Adaptive Simulation of Unsteady Reactive Flow (A-SURF) [13,45,46], is used and the governing equations for gas phase and liquid phase are shown below.

2.1.1. Gas phase

The conservation equations including the unsteady Navier-Stokes equations as well as energy and species mass fraction equations in a planar coordinate are given by

$$\frac{\partial U}{\partial t}+\frac{\partial F(U)}{\partial x}=F_v(U)+S_R+S_L, \tag{1}$$

where t and x are the temporal and spatial coordinates, respectively. The vectors U, $F(U)$, $F_v(U)$, S_R and S_L are defined as:

$$U=\begin{pmatrix}\rho Y_1\\ \rho Y_2\\ \vdots\\ \vdots\\ \rho Y_n\\ \rho u\\ E\end{pmatrix},\ F(U)=\begin{pmatrix}\rho u Y_1\\ \rho u Y_2\\ \vdots\\ \vdots\\ \rho u Y_n\\ \rho u^2+P\\ (E+P)u\end{pmatrix},\ F_v(U)=\begin{pmatrix}-(\rho Y_1 V_1')_x\\ -(\rho Y_2 V_2')_x\\ \vdots\\ \vdots\\ -(\rho Y_n V_n')_x\\ \tau_x\\ q_x\end{pmatrix},$$

$$S_R=\begin{pmatrix}\omega_1\\ \omega_2\\ \vdots\\ \vdots\\ \omega_n\\ 0\\ 0\end{pmatrix},\ S_L=\begin{pmatrix}S_{m,1}\\ S_{m,2}\\ \vdots\\ \vdots\\ S_{m,n}\\ S_v\\ S_e\end{pmatrix}. \tag{2}$$

Here the subscript x in $F_v(U)$ denotes the partial derivative with respect to the spatial coordinate x. ρ is the density, u is the flow velocity, Y_k, V_k', and ω_k are the mass fraction, diffusion velocity and production rate of species k, respectively. n is the number of species in gas phase. The production rate ω_k is specified via collection of elementary reactions using the CHEMKIN package [47]. The diffusion velocity V_k' is calculated by the mixture-averaged method. The pressure can be obtained from the density, temperature and mean molecular weight using $P=\rho RT/\bar{M}$, where $R=8.314$ J/(mol K). The viscous stress τ is represented by $\tau=2\mu\partial u/\partial x-2/3\bullet\mu\partial u/\partial x$, where μ is the dynamic viscosity of the gaseous mixture. E is the total energy and q is the heat flux (readers can refer to Refs. [13,45,46] for their detailed expressions). Note that the continuity equation is not included, because it can be recovered from the summation of all species mass fraction equations.

The full coupling between gas and liquid phases is taken into consideration in this work. Therefore, in the vector S_L in Eq. (2), the evaporation related source terms of species mass fraction (S_m), momentum (S_v) and energy (S_e) from liquid phase are given as

$$\begin{cases}S_m=N_d\dot{m}\\ S_v=-N_d m_d\frac{u-u_d}{\tau_r}\\ S_e=-N_d\left[hA_d(T-T_d)+\dot{m}L_v\right]\end{cases} \tag{3}$$

where $\dot{m}$, m_d, u_d and T_d are the evaporation rate, mass, velocity and temperature of a single droplet, respectively. N_d is the droplet number density. τ_r the droplet momentum relaxation time (given in Eq. (13)), h the convective heat transfer coefficient, A_d the surface area of the droplet. The latent heat of evaporation L_v is assumed to be constant in this work and equal to its value at the boiling point. The liquid source term for species k, $S_{m,k}$, is zero except when we consider the water (i.e. $S_{m,H_2O}=S_m$).

2.1.2. Liquid phase

In the current work, the Eulerian approach is introduced into the A-SURF code [13,45,46] to describe the liquid phase dispersed in continuous gas phase. The water droplet is spherical, and the temperature within each droplet is assumed to be uniform [48–50]. The droplet-droplet interactions and therefore the resultant droplet-related diffusion are neglected due to the dilute droplet loading of interest in our work [48–50]. The movement of the droplets is affected only by the drag force, without any external body forces (e.g. gravity), while the mass transfer rate between continuous phase and dispersed phase is estimated from the evaporation rate [51]. These simplifications were also used in previous studies of gas-droplet reaction systems [52,53]. The Eulerian models were also used, e.g. by Aggarwal and Sirignano [54] and Qiao [55], to describe dispersed solid carbon particle or liquid droplet phase in one-dimensional two-phase flames and reasonable results were obtained in terms of particle dynamics and critical gaseous flame phenomena. Below we present the governing equations of dispersed liquid phase for mass, momentum, energy and number density in the Eulerian framework and 1D planar coordinate system.

The evolution of the droplet diameter can be derived from the mass conservation equation:

$$\frac{\partial d}{\partial t}+u_d\frac{\partial d}{\partial x}=-\frac{2\dot{m}}{\pi\rho_d d^2}, \tag{4}$$

where d is the droplet diameter, ρ_d is the density of the droplet, and u_d is the velocity of the droplet phase. The evaporation rate $\dot{m}$ can be modelled as [51]

$$\dot{m}=\pi d\rho D_{water,m}\widetilde{Sh}\ln(1+B_M). \tag{5}$$

Here $D_{water,m}$ is the binary diffusion coefficient of water vapour in the gas-phase mixture. $\widetilde{Sh}$ is the Sherwood number [56,57]

$$\widetilde{Sh}=2.0+0.6Re_d^{1/2}Sc^{1/3}, \tag{6}$$

where Re_d is the droplet Reynolds number and Sc is the Schmidt number

$$Re_d=\frac{\rho_d d\,|u-u_d|}{\mu}, \tag{7}$$

$$Sc=\frac{\mu}{\rho D_{water,m}}. \tag{8}$$

In Eq. (5), B_M is the Spalding mass transfer number (Y_{ds} and $Y_{d\infty}$ are the mass fractions of water vapour at the droplet surface and the surrounding gas, respectively), i.e.

$$B_M=\frac{Y_{ds}-Y_{d\infty}}{1-Y_{ds}}, \tag{9}$$

$$Y_{ds}=\frac{W_{H_2O}X_{ds}}{W_{H_2O}X_{ds}+(1-X_{ds})\bar{W}}. \tag{10}$$

X_{ds} is the mole fraction of water at the droplet surface and is further derived from the Clausius-Clapeyron equation

$$X_{ds} = \frac{P_{ref}}{P} exp\left[\frac{L_v}{R}\left(\frac{1}{T_{ref}} - \frac{1}{T_d}\right)\right] \tag{11}$$

where P_{ref} and T_{ref} are reference pressure and temperature, respectively. W_{H_2O} is the molecular weight of the water and $\bar{W}$ is the molecular weight of the dry gas-phase mixture (excluding H_2O vapour). For water, P_{ref} = 1atm, T_{ref} = 370K, L_v = 2260J/g.

As mentioned before, inter-droplet interactions and gravity are neglected, the drag force only affects the droplet movement. The motion of droplet is determined by Newton's second law, considering the drag forces resulting from velocity slip between the two phases, and is governed by

$$\frac{\partial u_d}{\partial t} + u_d\frac{\partial u_d}{\partial x} = \frac{F_s}{m_d} = \frac{u - u_d}{f\tau_r}. \tag{12}$$

Here F_s is the drag force applied to a single droplet, and $m_d = \rho_d \pi d^3/6$ is the mass of a single droplet. τ_r is the momentum relaxation time and can be estimated as below based on the low Stokes number assumption, i.e.

$$\tau_r = \frac{\rho_d d^2}{18\mu_g}, \tag{13}$$

In Eq. (12), f is the drag function, which can be modelled with the Schiller and Naumann model [58]

$$f = \frac{24}{C_d Re_d}, \tag{16}$$

where C_d is the drag coefficient and, for spherical droplets, it can be modelled as

$$C_d = \begin{cases} \frac{24}{Re_d}\left(1 + \frac{1}{6}Re_d^{2/3}\right), & if Re_d < 1000 \\ 0.44, & if Re_d > 1000 \end{cases} \tag{17}$$

The droplet temperature T_d is obtained by solving the energy equation

$$m_d C_{P,d}\left(\frac{\partial T_d}{\partial t} + u_d\frac{\partial T_d}{\partial x}\right) = hA_d(T - T_d) - \dot{m}L_v, \tag{18}$$

where $C_{P,d}$ is the heat capacity of the water droplet. The heat transfer coefficient h can be estimated from Nusselt number Nu using the correlation from Rans and Marshall model [56,57], i.e.

$$Nu = \frac{hd}{k_g} = \frac{ln(1 + B_T)}{B_T}(2.0 + 0.6Re_d^{1/2}Pr^{1/3}), \tag{19}$$

where k_g is the thermal diffusivity of gas phase, $Pr = C_{P,g}\mu/k_g$ is the Prandtl number of the gas phase, $C_{p,g}$ is the heat capacity of the gas phase. B_T is the Spalding heat transfer number, and follows the relation as $B_T = (1 + B_M)^{\varphi} - 1$, in which $\varphi = (C_{p,v}/C_{P,d})/Le$ and Le is the Lewis number of the gaseous mixture. For simplicity, $B_T \approx B_M$ is adopted here, through assuming that unity mixture Lewis number Le and equal capacities for water vapour and droplet, i.e. $C_{p,v} \approx C_{P,d}$ [59]. This assumption is acceptable for the investigated stoichiometric n-heptane/air mixture and water properties.

Based on conservation of the total number of droplets in the system, the equation of droplet number density N_d reads

$$\frac{\partial N_d}{\partial t} + \frac{\partial(N_d u_d)}{\partial x} = 0. \tag{20}$$

2.2. Numerical method

Governing equations of gas phase (i.e. Eq. 1) and liquid phase (i.e. Eqs. 4, 12, 18 and 20) are solved in A-SURF [13,45,46]. For the gas phase equation, the second-order accurate, Strang splitting fractional-step procedure [60] is adopted to separate the time evolution of the stiff reaction term from that of the convection and diffusion terms. The non-reactive flow is solved in the first fractional step. Runge–Kutta, MUSCL-Hancock and central differencing schemes, all with second order accuracy, are employed to calculate temporal integration, convective flux and diffusion flux, respectively. In the second fractional step, the chemistry is solved using the VODE solver [61]. For the liquid phase equations, semi-analytical method, instead of any ODE solver, is used to solve Eqs. (4), (12), (18) and (20). Both phases are solved on the same mesh and with consistent time step in A-SURF. A multi-level, dynamically adaptive mesh refinement algorithm [62] is applied to ensure adequate numerical resolutions of the propagating flame front, end-gas autoignition and pressure waves [13,16]. Furthermore, two-way coupling in terms of mass, momentum, energy and species is conducted between two phases for each time step. These couplings are enforced through the source terms in Eq. (3) for the gas phase equations and also the terms at the right-hand side of droplet equations in Eqs. (4), (12) and (18).

2.3. Physical model

The physical model of the one-dimensional closed reactor is shown in Fig. 1. The computational domain is $0 \le x \le L$, and L = 5 cm is the reactor length. For gas phase, the initial pressure P_0 is 40 atm in the reactor and the initial flow is static (i.e. u_0 = 0 m/s). A hot spot at the left boundary is introduced, aiming to initiate a reactive front in the end gas. Specifically, it is modelled by a linear temperature distribution with negative gradient

$$T_0(x) = T(t = 0, x) = \begin{cases} T_m + \left(x - \frac{x_s}{2}\right)\frac{dT_0}{dx}, & for \quad 0 \le x \le x_s \\ T_m + \frac{x_s}{2}\frac{dT_0}{dx}, & for \quad x > x_s \end{cases}, \tag{21}$$

where x_s = 5 mm is the hot spot size, T_m = 1000 K is the initial local temperature at $x = 0.5x_s$, $\frac{dT_0}{dx} = -1.0$ K/mm is the negative temperature gradient inside the hot spot, and T_0 = 997.5 K is the initial temperature in the reactor. This hot spot is to mimic the localized thermal inhomogeneity in the reactor, which can be practically generated by various factors in the IC engine chamber, e.g. hot gas residual or near-wall heating. Based on Zel'dovich [6], the linear temperature can induce an autoignition reactive front due to the distribution of the local ignition delay time. The propagation speed u_a can be correlated to the gradient of the ignition delay time τ as

$$u_a = \left(\frac{d\tau}{dx}\right)^{-1} = \left(\frac{d\tau}{dT_0}\frac{dT_0}{dx}\right)^{-1}. \tag{22}$$

When the autoignition front moves at the sound speed a, detonation can occur through the coupling with the pressure wave generated from

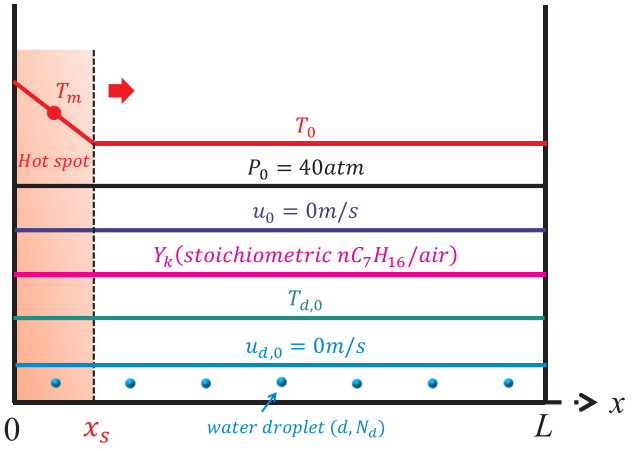

Fig. 1. Schematic of hot spot for autoignition in n-heptane/air with water droplet in a 1D closed reactor with the length of L.

the local heat release because of their mutual reinforcement. The temperature gradient at which $u_a = a$ is defined as the critical temperature gradient $(dT_0/dx)_c$, i.e.

$$\left(\frac{dT_0}{dx}\right)_c = \left(\frac{d\tau}{dT_0}a\right)^{-1} \tag{23}$$

Based on our previous 0D homogeneous ignition calculations of droplet-free n-C_7H_{16}/air mixture at $P_0 = 40$ atm with the same chemical mechanism [63], the critical temperature gradient is approximately -0.4 K/mm [13]. Therefore, the current temperature gradient $dT_0/dx = -1.0$ K/mm considered in this work is sufficient to generate a reactive front from the hot spot, which can finally evolve into the detonation wave in the droplet-free n-C_7H_{16}/air mixture. We can hence further investigate the effects of the water droplet on the propagation of the propagating reaction front and end gas autoignition.

For liquid phase, the initial temperature of the droplet is 298 K and the water droplet is stationary at the beginning (i.e. $u_{d,0} = 0$ m/s). The droplets introduced in this study is to mimic the water mists injected into the engine chamber to mitigate the knock and reduce NOx emissions, or the residual water droplets in the end gas due to the hydrous fuel sprays [5]. Different initial droplet diameters d and number densities N_d will be considered in this work, to examine their influences on autoignition and detonation front evolutions in n-heptane/air mixture. Note that the selections of d and N_d follows the spray characteristics relevant to IC engine conditions, and meanwhile they are still not dense and therefore the inter-droplet collision is not dominant. Furthermore, adiabatic and reflective boundary conditions are adopted for both boundaries $x = 0$ and $x = L$.

The skeletal chemical mechanism for n-heptane oxidation [63] is used in our simulations. It consists of 44 species and 112 elementary reactions. This mechanism has been shown to be able predict autoignition and flame propagation in n-heptane/air mixtures at a broad range of temperature and pressure [12–16].

3. Results and discussion

3.1. Autoignition and detonation development

Fig. 2a and b compare the transient processes of detonation development without and with droplets, respectively. For the purely gaseous case (baseline case), Fig. 2a shows that Lines #1–2 correspond to the detonation development process. At Line #2, the reactive front evolves into a detonation wave with high pressure, temperature and a rapid increase in heat release rate. After that, the self-sustaining detonation wave propagates to the right until thermal explosion occurs in the unburned mixture. The averaged detonation speed between Lines #2 and #3 is 1,816 m/s, which is close to 1,845 m/s, the Chapman–Jouguet detonation speed for stoichiometric n-C_7H_{16}/air at $T_0 = 997.5$ K and $P_0 = 40$ atm. For Lines #3–5, the detonation wave gradually degenerates into a shock wave, which continues propagating to the right. No autoignition occurs at the right end throughout the whole process (Lines #1–5). Similar phenomena in droplet-free n-heptane/air mixture with temperature gradient were also observed in Refs. [9,13,14].

Fig. 2b shows the counterpart results based on the same n-heptane/air mixture as in Fig. 2a, but with water droplets of $d = 30$ μm and $N_d = 30{,}000$ cm^{-3} (case 1). The time sequences in Fig. 2a and b demonstrate that the presence of the water droplets with the above properties delays the occurrence of initial autoignitive wave, detonation, degraded shock wave and thermal explosion. In the current case, this delay is mainly caused by the slow formation of the initial autoignition wave from the hot spot. However, this delay effect is not markedly seen for the timing corresponding to detonation development and propagation, as well as thermal explosion. The evaporation cooling effects are further confirmed through the extra numerical tests with droplet evaporation but without chemical reactions. It is shown that within the studied detonation development period (about 660 μs in Fig. 2b), reduction of the gas temperature is approximately 10 K. Therefore, such small temperature reduction would not demonstrate significant influences on the end gas combustion evolutions, but may sufficiently change the hot spot reactivity. Furthermore, during the detonation propagation process (Lines #2–3) in Fig. 2b, the peak values of pressure and heat release rate are considerably lower than those in Fig. 2a. The detonation propagation speed is also smaller in Fig. 2b (1767 m/s, an average value estimated from Lines #2 and #3) than that in Fig. 2a. These also indicate the suppression effect of the dispersed droplets on the reaction wave development in the end gas with localized hot spot. Also, based on the stand-alone numerical experiments without hot spots for both baseline case and case 1 (which are equivalent to 0D homogeneous ignition modelling), only thermal explosions occur without generation of the spontaneous propagating waves.

Fig. 3 shows the temporal evolutions of pressure, temperature and heat release rate for case 2 with increased droplet diameter $d = 50$ μm at the same number density $N_d = 30{,}000$ cm^{-3} as in Fig. 2b. Compared with the results of case 1 in Fig. 2b, it takes a longer time for the

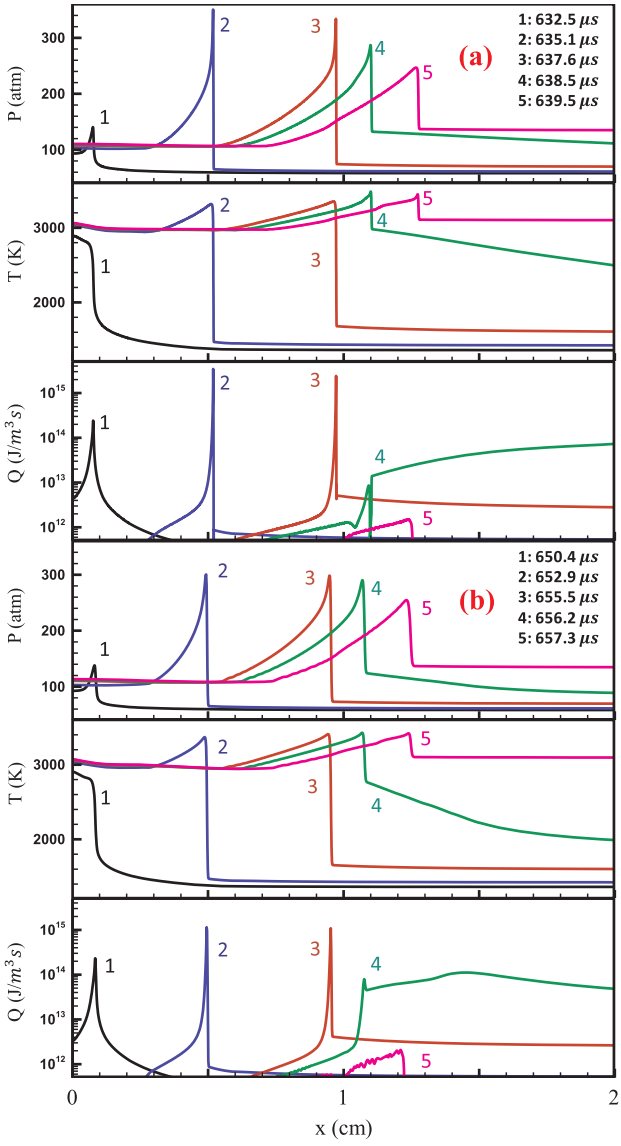

Fig. 2. Temporal evolutions of pressure, temperature and heat release rate distributions in (a) baseline case and (b) case 1 with $d = 30$ μm, $N_d = 30{,}000$ cm^{-3}.

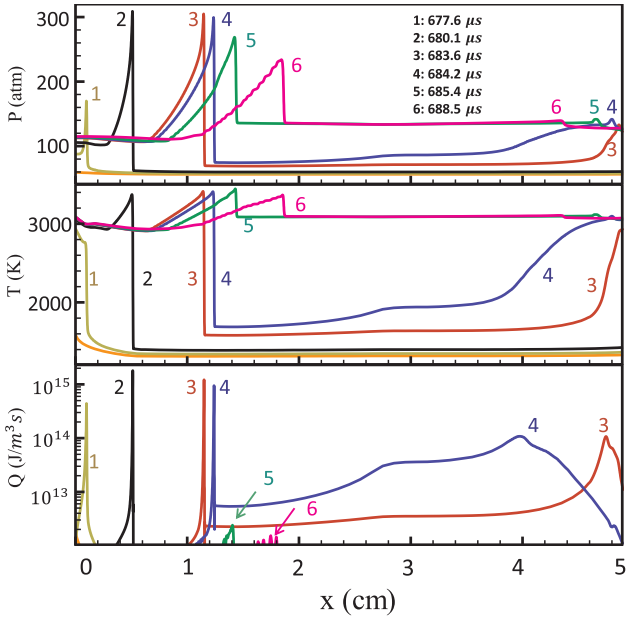

Fig. 3. Temporal evolutions of pressure, temperature and heat release rate distributions in case 2 with d = 50 μm and N_d = 30,000 cm^{-3}.

autoignitive fronts to be generated in and move beyond the hot spot at the left boundary. The time difference between Figs. 3 and 2b is around 27.2 μs. Then, the evolutions of the reaction fronts originated from the left hot spot are qualitatively similar to the results in Fig. 2b, as shown in Lines #1–6. Nevertheless, relative to the respective Line #1, in Fig. 3, this process takes about 11 μs, longer than that in Fig. 2b (around 7 μs from Line #1 to Line #5 therein). Furthermore, the detonation propagation speed is 1831 m/s, 3.6% higher than that in Fig. 2b.

Interestingly, a new autoignitive front arises (see Line #3 in Fig. 3) at the right boundary, as shown in Fig. 3. The high temperature from this new front leads to partial reaction in front of it, as shown in Line #4. Ultimate thermal explosion in the rest of the end gas occurs when the local ignition delay is reached, and hence no interactions between the reaction fronts from two boundaries are observed. It should be noted that, relative to Line #1, here the thermal explosion time occurs at about 10.9 μs, roughly doubling the value in Fig. 2b (i.e. 6.9 μs). Therefore, the effects of increased initial diameter of the dispersed droplets on the reaction front developments are substantial (e.g. slow down the formation of the left autoignition front, speed up the detonation front propagation, and induce the new right front), which drives us to further examine how they respond to larger droplets.

Fig. 4 shows the results for case 3 with d = 100 μm and N_d = 30,000 cm^{-3}. Comparing with Fig. 3, the following distinctions should be highlighted about the reaction front from the left hot spot: (1) slower formation of reaction fronts from the hot-spot; (2) higher peak pressures and (3) variable detonation propagation speeds. For the left detonative front, the speeds are 1919, 2000 and 1835 m/s, respectively, estimated from Lines #2 to #5. Overall, these speeds are higher with various levels than that from Fig. 3 (i.e. 1831 m/s). This may be caused by the fact that the dispersed water droplets to some degree reduce the actual initial temperature gradient within the hot spot, and therefore the spontaneous reaction front generated from there can propagate into the end gas at a higher speed [6]. At Line #3, approximately 9 μs after Line #1, a right autoignition front arises, and then quickly evolves into a left-propagating detonation wave (Line #4). Therefore, due to the fast transition into the detonation wave (less than the local ignition delay of the end gas between two fronts), thermal explosion does not appear in this case. From Lines #4–6, both detonation waves propagate in an opposite direction and finally collide with each other at $x \approx$ 3.0cm, leading to a superhigh pressure with a magnitude of over 750 atm. All the end gas has been consumed and the two detonation waves degenerate and permeate through each other (Line #7).

Fig. 5 further shows the results for case 4 with increased number density, N_d = 50,000 cm^{-3}, with the same droplet diameter d = 100 μm as in Fig. 4. Like the results in Figs. 3 and 4, two oppositely travelling reaction fronts are generated from the left and right boundaries, respectively, although these occur much later (over 200 μs) than the counterparts in Fig. 4. Based on Lines #1 and #2, the average propagating speeds of the left and right fronts are about 35 m/s and 56 m/s, respectively. Nonetheless, the right front becomes detonative as shown in Line #3, whereas the left one (see Line #4) also develops into the detonative front about 5 μs later than the right one. Although detonation waves are seen in both Figs. 4 and 5, nevertheless, when the droplet number density is increased, their occurrence is considerably delayed: in Fig. 5, it is 1,250 μs, much longer than 786.3 μs in Fig. 4. Meanwhile, they are present in the middle section of the reactor, instead of the left and right boundaries as shown in Figs. 3 and 4.

The modes of end-gas autoignition and detonation development shown in Figs. 2–4 (i.e. cases 1–3) are also seen in Yu et al. [16] and Pan et al. [18]. In the cases studied by Yu et al. [16], decrease in ignition delay time (by increasing the initial temperature or pressure) and increase in flame propagation time (by increasing the chamber length) both help to induce end-gas autoignition. Pan et al. [18] demonstrated the essential role of pressure wave disturbance in the formation of thermal inhomogeneity and detonations. However, the new mode of case 4 (see Fig. 5) is not observed from the previous studies. Therefore, in the present study dealing with the two-phase system, the end-gas autoignition may result from the evaporation rate inhomogeneity that causes the non-uniform thermodynamic state of the end gas (will be further discussed in Section 3.3).

3.2. Droplet dynamics

To further unravel the droplet dynamics in two-phase detonative combustion, Fig. 6 shows the distributions of droplet number density, droplet evaporation rate and diameter at different instants from case 1. Considerable deviations from the initial N_d (30,000 cm^{-3}) can be seen in Fig. 6a, and distributions of N_d resemble single-periodic sine-waves. In general, the droplets move and are accumulated after the gaseous reaction fronts (denoted with open circles along the top x-axis).

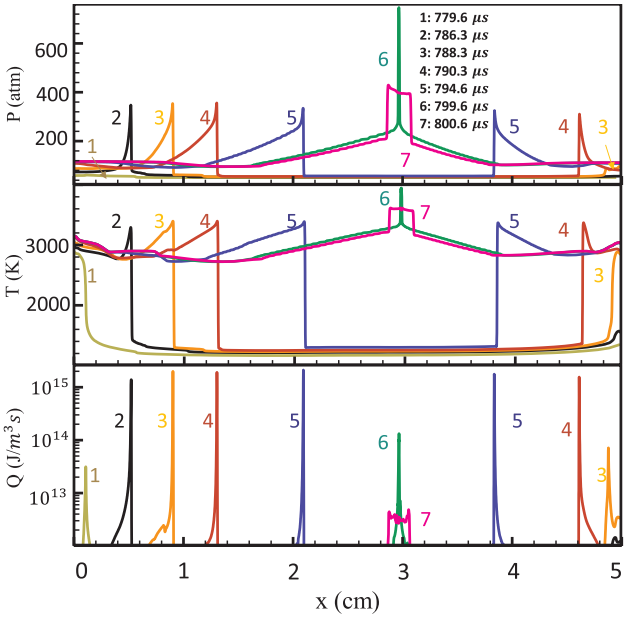

Fig. 4. Temporal evolutions of pressure, temperature and heat release rate distributions in case 3 with d = 100 μm and N_d = 30,000 cm^{-3}.

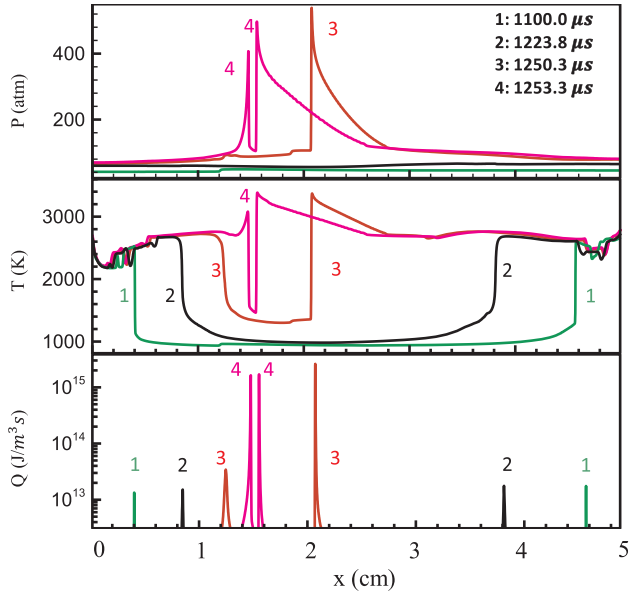

Fig. 5. Temporal evolutions of pressure, temperature and heat release rate distributions in case 4 with $d = 100$ μm and $N_d = 50{,}000$ cm^{-3}.

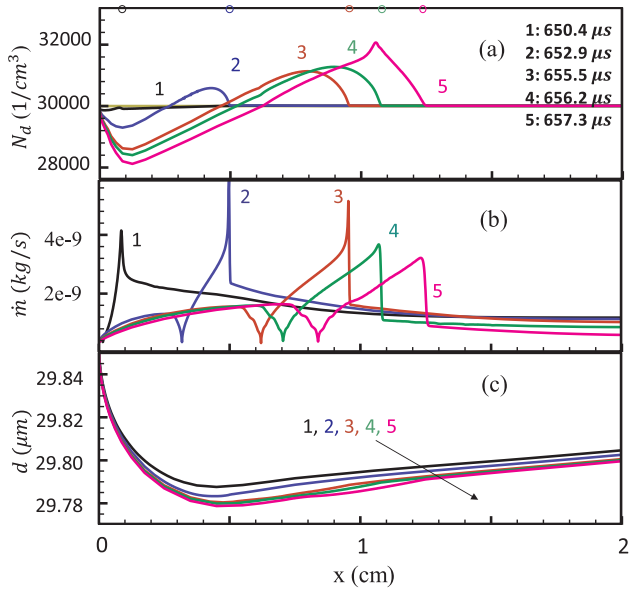

Fig. 6. Temporal evolutions of (a) droplet number density, (b) evaporation rate and (c) droplet diameter distributions for case 1. The open circles along the upper horizontal axis indicate the reaction front locations in gas phase at the shown instants (same color, same instant).

However, the locations with maximum number densities fall well behind the reaction fronts. This implies the pronounced inertial of the finite-sized droplets (30 μm in case 1). Close to the left boundary, the local number density is below the initial value, indicating the reduction of the droplet number there due to their movement caused by the propagating gas phase. Fig. 6b shows that the effects of reaction front development on droplet evaporation are significant. The evaporation rate $\dot{m}$ is non-monotonic behind the detonation/shock waves. Note that here $\dot{m}$ is estimated from the single droplet evaporation rate model (see Eq. (5)), based on local gas and liquid phase properties. For instance, based on Line #3, in the detonated or shocked gas, from $x = 0$, $\dot{m}$ gradually increases, and at around $x = 0.6$ cm, it reaches a minimum value. Then it sharply goes to the peak value, where the detonation front exists. In what follows, we term this distribution of $\dot{m}$ as M-shaped profile with left mild and right spiky maxima (e.g. Line #3). When the detonation is weakened into a shock wave (Lines #4 and #5), the evaporation rate distributions are still M-shaped, but the right peak values of evaporation rate $\dot{m}$ decreases accordingly. We will further discuss the intrinsic mechanism for this non-monotonicity behavior of $\dot{m}$ in Fig. 7. Moreover, the droplet diameter d in Fig. 6c shows obvious change in Lines #1–5. Overall, strong $\dot{m}$ leads to the lower diameter, but the droplets are still far from being completely vaporized and their diameters only decrease by less than 1% due to the relatively low evaporation rate of water sprays.

To understand the mechanism for droplet evaporation during reaction front propagation, we plot the distributions of key quantities related to evaporation rate $\dot{m}$ for two stages, i.e. before and after detonation is initiated from the hot spot. At early stage (before detonation), the droplet temperature (see Fig. 7b) is below the boiling point of liquid n-heptane. In the reactor $0 \le x \le 5$ cm, the higher the droplet temperature T_d, the higher n-heptane vapor concentration X_{ds} (see Eq. 11) at the droplet surface, which lead to higher Spalding mass transfer number B_M (see Eq. 9) and therefore larger evaporation rate $\dot{m}$ (see Eq. 5). Hereafter, for brevity, we call this mechanism as Spalding number effect due to the droplet temperature. Furthermore, currently the droplet velocity is smaller than the gas velocity, although both of their magnitudes are small. The existence of such finite velocity difference would lead to finite Reynolds numbers Re_d (Eq. 7) as plotted in Fig. 7a. The increased droplet Reynolds number Re_d would result in increased Sherwood number $\widetilde{Sh}$ (Eq. 6), thereby enhancing the evaporation rate. This is termed as droplet Reynolds number effect hereafter. In this stage, the variations of pressure (not shown here) are still negligible, and therefore their influences on $\dot{m}$ are comparatively limited. One can see that, before detonation occurs, the evaporation is jointly affected by Spalding number effect due to droplet temperature and droplet Reynolds number effect, both of which facilitate the droplet evaporation in the present case.

When detonation occurs, the droplet has reached the boiling point temperature (see T_d in Fig. 7b), and therefore T_d is not a variable any more directly affecting the local $\dot{m}$. In reality, the Spalding mass transfer number B_M in Fig. 7b is mainly influenced by the local pressure (see Line #3 in Figs. 2 and 6b). Through Eqs. (5)–(11), one can find that higher gas pressure surrounding the droplet would reduce the vapor concentration at the droplet surface X_{ds}, and accordingly the Spalding mass transfer number B_M, and therefore decrease the evaporation rate $\dot{m}$. We call this as Spalding number effect due to the local gas pressure. Based on Fig. 7a, the gas velocity u goes very high due to the detonation, and is much higher than droplet velocity u_d. This directly results in high droplet Reynolds number (see Fig. 7a). Close to the hot spot boundary, the velocities of two phases are equal, leading to $Re_d = 0$. At $x = 0$, their velocity differences are relatively small and hence finite Re_d is seen. Generally, between $x = 0$ and the detonation front, the distributions of Re_d are M-shaped (see the right figure of Fig. 7a). Overall, in this stage, droplet Reynolds number effect increases $\dot{m}$, whilst Spalding number effect due to the high pressure suppresses the evaporation of the water droplets. In addition, the former effect dominates the latter, as shown in Fig. 7. Now this justifies the M-shaped $\dot{m}$ profiles seen in Figs. 6b and 7c.

Fig. 8 shows the droplet properties for case 2 ($d = 50$ μm and $N_d = 30{,}000$ cm^{-3}) at the same five instants as shown in Fig. 3. Fig. 8a shows that the distributions of droplet number densities are similar to case 1 in Fig. 6. Note that although auto-ignitive front arises from the right boundary, the distributions of N_d close to $x = 5$ cm are almost intact. Also, as shown in Fig. 8b, the droplet evaporation rate distributions in the left domain for case 2 are generally similar to those of case 1 in Fig. 6b. The corresponding mechanisms have been explained in Fig. 7. However, in Lines #3 and #4, between the central minimum and right maximum values in the M-shaped profiles, there is another maximum $\dot{m}$ (e.g. $x = 1$ cm at Line #3). It should be emphasized that

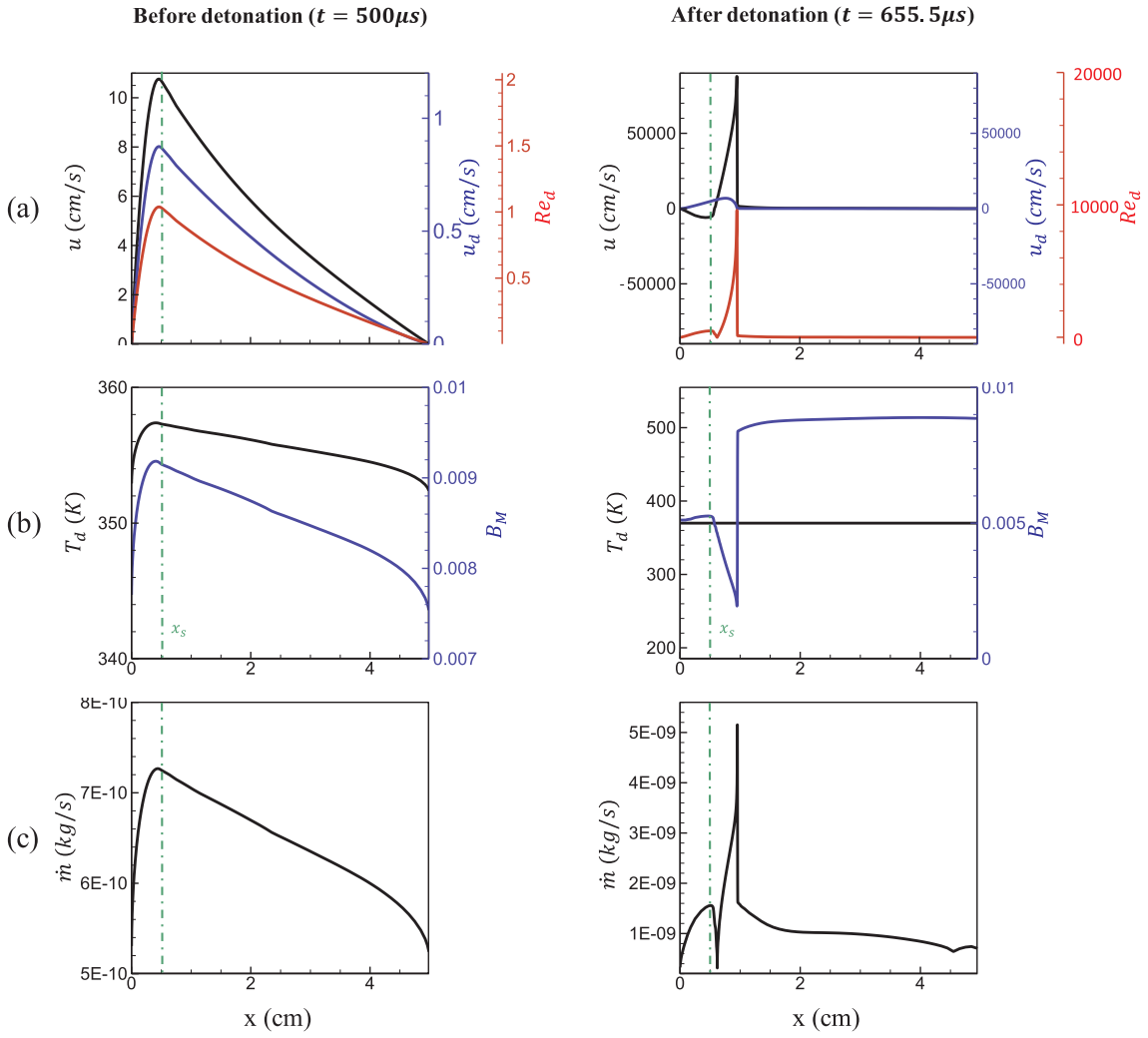

Fig. 7. Distributions of (a) gas, droplet velocities and droplet Reynold number, (b) droplet temperature and Spalding mass transfer number, and (c) evaporation rate for case 1 before ($t = 500\ \mu s$) and after ($t = 655.5\mu s$) the detonation is initiated. The green dash-dotted lines represent the hot spot boundary. (For interpretation of the references to color in this figure legend, the reader is referred to the web version of this article.)

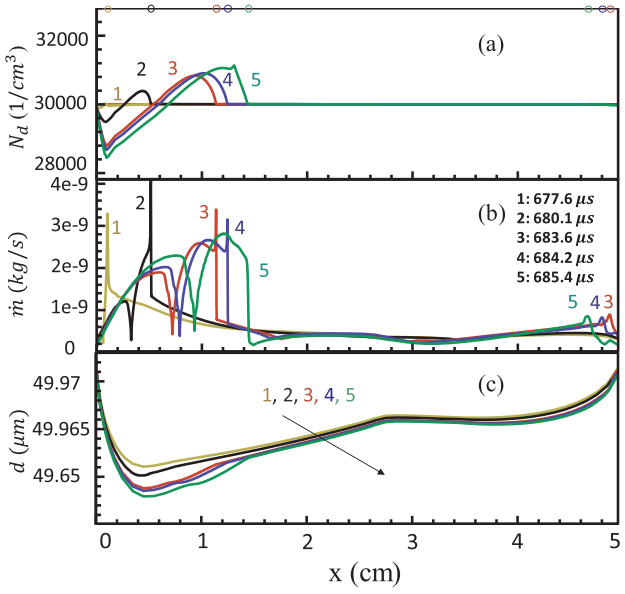

Fig. 8. Temporal evolutions of (a) droplet number density, (b) evaporation rate and (c) droplet diameter distributions for case 2. See the implications for the open circles in Fig. 6.

the droplet temperature has not reached the boiling point for all the lines in Fig. 8. For Line #3, at $x = 1$ cm, the droplet temperature is relatively high (due to the heating from the detonative fronts) but still lower than the boiling point (the distributions are not shown here), and this directly leads to the local increase of droplet evaporation rate in the *M*-shaped profiles, which corresponds to the foregoing Spalding number effect due to the droplet temperature T_d. However, this extra maximum of the evaporation rate $\dot{m}$ is not found in case 1 (see Fig. 6), since when the detonation occurs the droplet has reached boiling point in the entire reactor due to its smaller diameter. Furthermore, the finite evaporation rates are also observed near the right boundary (see Lines #3-#5), but much lower than those in the left domain. This is because only deflagrative fronts are generated and the corresponding gas and droplet temperatures are comparatively lower than that at the left boundary, which has been shown in Fig. 3. Owing to the high value of $\dot{m}$, decrease of the droplet diameter in the left domain (see Fig. 8c) is more pronounced than in the right domain.

Similarly, Fig. 9 shows the droplet properties for case 3 ($d = 100$ μm and $N_d = 30{,}000\ \text{cm}^{-3}$) at the same instants as in Fig. 3. In Lines #1, #2 and #3, the distributions of N_d and $\dot{m}$ are qualitatively similar to the earlier results in Figs. 6 and 8. When the two detonation waves collide at $t = 799.6$ μs (see Line #6 in Fig. 4), the peak droplet number density arises at $t = 799.6$ μs (see Line #4 in Fig. 9a), implying the substantial accumulation of the oppositely moving droplets

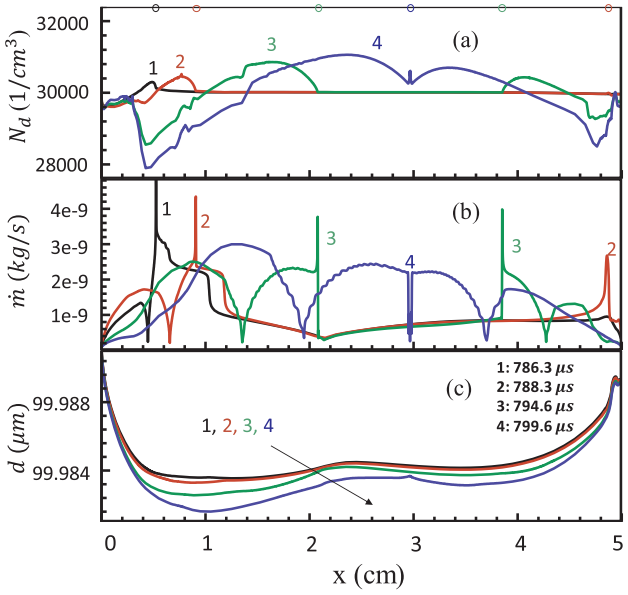

Fig. 9. Temporal evolutions of (a) droplet number density, (b) evaporation rate and (c) droplet diameter distributions for case 3. See the implications for the open circles in Fig. 6.

following the gas mixture. In the detonated region, the *M*-shaped profiles for $\dot{m}$ are noticeable. Interestingly, in Fig. 9b, the striking difference from the results in Fig. 6b and 8b is the considerably suppressed evaporation rate $\dot{m}$ near the collision location (i.e. around $x = 3$ cm in the reactor), where superimposition of high pressures from detonation waves occurs. The local superhigh pressure magnifies the effects from the Spalding number effects, thereby suppressing the local droplet evaporation at around $x = 3$ cm.

Plotted in Fig. 10 are the profiles of droplet number density, evaporation rate and diameter for case 4 ($d = 100$ μm and $N_d = 50{,}000$ cm^{-3}). For Lines #1 and #2 in Fig. 10a, since only deflagrative fronts are present for both sides based on Fig. 5, the distributions of N_d are relatively uniform in the entire domain. When the detonation fronts are developed in Lines #3 and #4, N_d shows larger variations. The lower N_d close to the two boundaries is probably caused by the propagating deflagrative fronts from them. Fig. 10b shows that, when the reaction fronts are deflagrative (see Lines #1 and #2), the evaporation rates are higher between the oppositely travelling fronts (i.e. in the unburned end gas) than in burned regions. In Lines #1 and #2, the *m*-shaped distributions of $\dot{m}$ arises and there is a minimum value, e.g. around $x = 2.4$ cm in Line #2. Once the detonation fronts appear in Lines #3 and #4, the profiles of the evaporation rate are *M*-shaped. Compared to the *M*-shaped of $\dot{m}$ distributions here and also in Figs. 6, 8 and 9, there are several differences we must mention for *m*-shaped $\dot{m}$ distributions when the two deflagrative fronts are present. Firstly, in this case, *m*-shaped profile lies in the end gas, instead of the detonated or shocked regions. Secondly, due to the deflagrative combustion here, no very localized spikes in the entire reactor are seen (therefore we symbolically call it *m*-shaped, instead of *M*-shaped); instead, two maxima (at around $x = 1.5$ and 3.2 cm in Line #2) are present with continuously changing $\dot{m}$.

The mechanism behind the *m*-shaped evaporation characteristics in the unburned zone of case 4, corresponding to the deflagrative front propagation in the reactor, will be future interpreted in Fig. 11. Fig. 11a and b respectively show the spatial profiles of velocities, droplet Reynolds number, droplet temperature and Spalding mass transfer number in the reactor. As shown in Fig. 5a, the pressure variation is relatively small due to the deflagrative combustion in Lines #1 and #2. Therefore, its effects on $\dot{m}$ is expected to be limited. Conversely, the droplet temperature T_d is still lower than the boiling temperature (see Fig. 11b), and generally it is high/low in the burned/unburned zone. This directly results in a high/low Spalding mass transfer number B_M in the burned/unburned zones. The velocity difference between two phases can be seen in Fig. 11a. For the gas phase velocity, its profile resembles a dual-periodic sine wave, which directly leads to the *m*-shaped distributions of droplet Reynolds number. Therefore, in this scenario, the droplet Reynolds number dominates in the droplet evaporation in fresh end gas region.

3.3. Further discussion

3.3.1. Formation of reaction fronts from the right boundary

As discussed above, the presence of the water droplets in the *n*-heptane/air mixture considerably changes the formation of the auto-ignitive fronts from the right boundary and their subsequent evolutions. The temporal evolutions of the pressure at the right boundary for the cases 1 – 4 are shown in Fig. 12a. The timing of a steep pressure wave occurrence at the wall increases with the droplet diameter and/or number density. For case 1, it is the thermal explosion (see Line #5 in Fig. 2b) that causes the rapid pressure to increase. Compared to case 1 without end-gas autoignition, the corresponding steep pressure value decreases from case 2 to case 4 with end-gas autoignition. After that, pressure oscillation is observed for cases 1–3, which is caused by the back-and-forth propagation of pressure waves in the closed reactor. For case 4, the strong evaporation effect suppresses the detonation development in the early stage and hence no significant oscillatory behavior is observed within 1200 μs.

To further reveal the formation of reaction fronts from the right boundaries, an Integral of dimensionless Temperature Difference (*ITD*) for identifying the mechanisms of hot spot generation is introduced [18,26]:

$$ITD(t) = \frac{1}{T_0}\int_0^t (T_{x=5.0} - T_{x=4.8})dt, \tag{24}$$

where T_0 is the initial temperature, $T_{x=5.0}$ is the temperature at the wall ($x = 5.0$ cm), $T_{x=4.8}$ is that at $x = 4.8$ cm in the reactor, and t is the elapsed time. Here, *ITD* can be regarded as an indicator of the accumulation of temperature difference between the above two points.

Fig. 12b shows the time histories of *ITD* for cases 1 – 4. The inhomogeneity of temperature distributions in the end gas region is

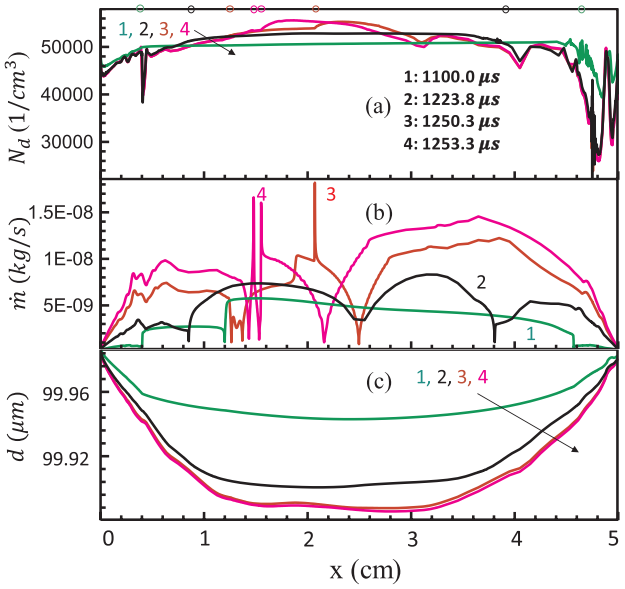

Fig. 10. Temporal evolutions of (a) droplet number density, (b) evaporation rate and (c) droplet diameter distributions for case 4. See the implications for the open circles in Fig. 6.

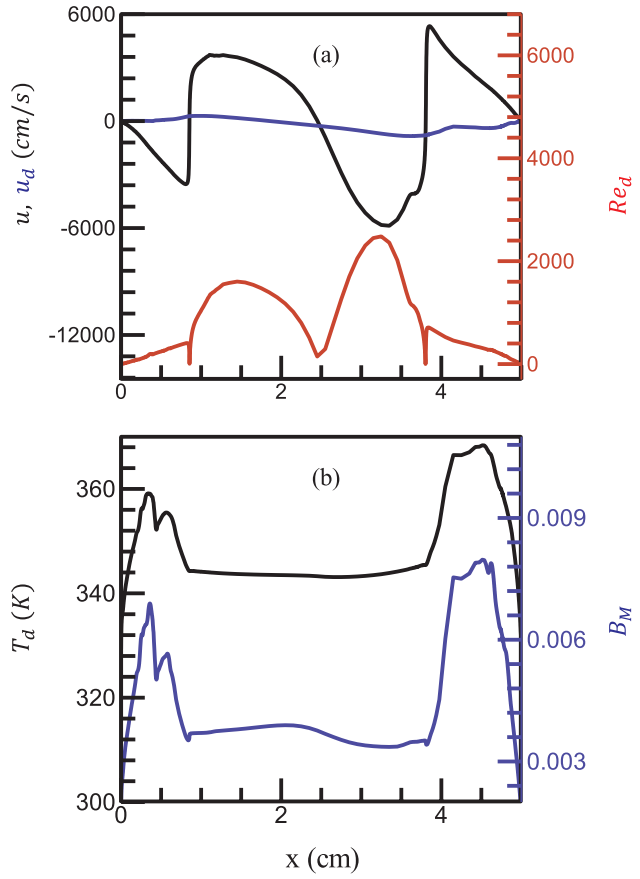

Fig. 11. (a) Gas, droplet velocities and droplet Reynold number, and (b) droplet temperature and Spalding mass transfer number for case 4 at t = 1223.8 μs (i.e. Line #2 in Fig. 10).

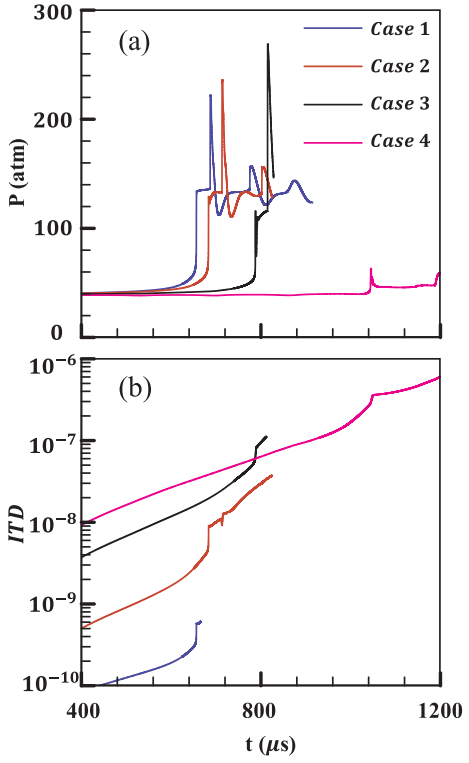

Fig. 12. Time histories of (a) pressure at the wall (x = 5.0 cm) and (b) integrals of dimensionless temperature differences.

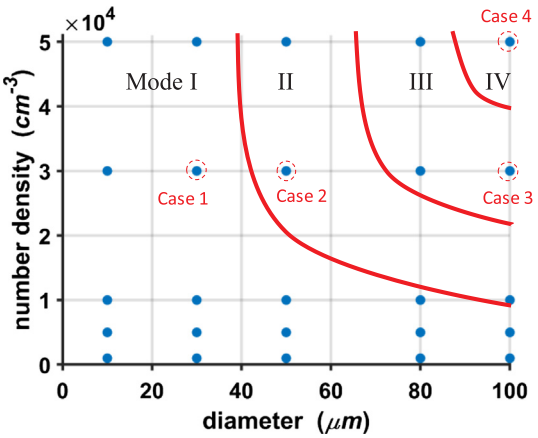

Fig. 13. Regime of four autoignition modes of droplet-laden *n*-heptane/air mixture in the space of d and N_d.

indicated by large *ITD*. Like pressure evolutions in Fig. 12a, the *ITD* increases slowly until a steep *ITD* occurs. Moreover, the result shows that the *ITD* of case 1 is relatively small, while for cases 2 – 4 the *ITD* increases with a longer ignition time and hence the gas at the wall becomes more reactive with higher temperature than that at the other point. As such, end-gas autoignition occurs on the right boundary for cases 2 – 4.

3.3.2. Regime of autoignition and detonation development

From the previous sections, four autoignition modes (corresponding to cases 1–4) can be observed for a hot spot with temperature gradient: I, detonation in the left boundary (Fig. 2); II, detonation in the left and deflagration in the right (Fig. 3); III, detonation in the left and right (Fig. 4); IV, deflagration in the left and right (Fig. 5). In the above analysis, only several representative droplet diameters and number densities are taken into consideration.

To get more general conclusion, simulations for a wide range of droplet diameters and number densities are further conducted. Fig. 13 summarizes the various modes in terms of d and N_d. In this regime map, the droplet diameter d ranges from 0 to 100 μm and the droplet number density ranges from 0 to 50,000 cm^{-3}. The range of d and N_d covers the modes (as from cases 1–4) we observed previously. Different modes are roughly separated by the red curves. When $d < 40$ μm or $N_d < 10^4$ cm^{-3}, Mode I is dominant. However, significant distinctions are observable if the droplet diameter or number density is varied when $d > 40$ μm and $N_d > 10^4$ cm^{-3}. Specifically, if the droplet diameter or number density is increased further, Mode II becomes important, as shown in the left ring-shaped zone in Fig. 13. Mode III can be observed if diameter and number density are changed to larger values (right ring-shaped zone). Case 4 discussed above lies at the corner in this N_d - d diagram, which corresponds to Mode IV. Generally, when the droplet diameter and/or number density are large, the autoignition and detonation development in the confined reactor become diversified.

It should be highlighted that Fig. 13 is obtained based on the stochiometric *n*-C_7H_{16}/air mixture with initial temperature of T_0 = 997.5K and pressure of P_0 = 40atm. Variations of the above initial conditions of the gaseous mixture may lead to change of the regime of autoignition and detonation development subject to the droplet properties. For example, vaporization of the water droplets would considerably affect the reactivity of the off-stoichiometric mixtures, and therefore lead to different autoignitive modes from those indicated by Fig. 13. Due to the intrinsic complexity of the two-phase reaction system, further systematic studies are needed which will be the topic of our future work.

4. Conclusions

One-dimensional two-phase simulations are conducted to study the autoignition modes and detonation development initiated by a hot spot in *n*-heptane/air mixture with water droplets in a planar reactor. A Eulerian-Eulerian framework is used to simulate multi-component, fully compressible and reactive multi-phase flows is developed. Full inter-phasic coupling is considered, in terms of mass, momentum and energy. The emphasis is laid on the influences of droplet properties (i.e. diameter and number density) on the development of reaction fronts in gas phase, as well as their evaporation characteristics under different combustion modes.

It is found that presence of water droplet considerably changes the reaction front development in the reactor. Four typical autoignition modes are identified with variable diameters and/or number densities: (I), detonation in the left side; (II), detonation in the left and deflagration in the right; (III), detonation in both sides; (IV), deflagration in both sides. Accordingly, a mode regime is plotted based on droplet diameter and number density. Additionally, the results show that the larger droplet diameter or number density leads to the later initiation of the reaction fronts from the hot spot and the thermal explosion in the end gas.

For the droplet evaporation features, various effects are identified, including droplet Reynolds number effect, Spalding number effects due to local gas pressure and droplet temperature. For the droplet Reynolds number effect, this is caused by considerable velocity difference between two phases and typically facilitates their evaporation for the droplets in the detonated or shocked gas. For Spalding number effects due to the local gas pressure, high local pressure (behind the detonation front or at the pressure wave collision location) would suppress the droplet evaporation. Before the droplet temperature reaches the boiling point, higher droplet temperature would lead to larger evaporation rate, which corresponds to the Spalding number effect. Our results show that at different stages of reaction front development, one or some of the effects will dominate in the water droplet evaporation. The non-monotonic distributions of droplet evaporation rates are seen, e.g. *M*-shaped profiles behind the detonation or shock waves.

Acknowledgements

YZ and QL are financially supported by Research Scholarship Budget from National University of Singapore (NUS). HZ is financially supported by the start-up grant (R-265-000-604-133) from NUS. PD is financially supported by grants (Nos. 51976088 and 51606091) from National Natural Science Foundation of China.

References

[1] Grogan KP, Goldsborough SS, Ihme M. Ignition regimes in rapid compression machines. Combust Flame 2015;162:3071–80.
[2] Heywood JB. Internal combustion engines fundamentals. New York: McGraw Hill; 1988.
[3] Bates L, Bradley D, Ron OI, Mon KRON. Deflagrative, auto-ignitive, and detonative propagation regimes in engines. Combust Flame 2017;175:118–22.
[4] Robert A, Richard S, Colin O, Poinsot T. LES study of deflagration to detonation mechanisms in a downsized spark ignition engine. Combust Flame 2015;162:2788–807.
[5] Zhu S, Hu B, Akehurst S, Copeland C, Lewis A, Yuan H, et al. A review of water injection applied on the internal combustion engine. Energy Convers Manage 2019;184:139–58.
[6] Zeldovich YAB. Regime classification of an exothermic reaction with nonuniform initial conditions. Combust Flame 1980;214:211–4.
[7] Im HG, Pal P, Wooldridge MS. A regime diagram for autoignition of homogeneous reactant mixtures with turbulent velocity and temperature fluctuations. Combust Sci Technol 2015;187:1263–75.
[8] Weber H, Mack A, Roth P. Combustion and pressure wave interaction in enclosed mixtures initiated by temperature nonuniformities. Combust Flame 1994;295:281–95.
[9] Gu XJ, Emerson DR, Bradley D. Modes of reaction front propagation from hot spots. Combust Flame 2003;133:63–74.
[10] Bradley D, Kalghatgi GT. Influence of autoignition delay time characteristics of different fuels on pressure waves and knock in reciprocating engines. Combust Flame 2009;156:2307–18.
[11] Bradley D. Autoignitions and detonations in engines and ducts. Philos Trans A Math Phys Eng Sci 2012;370:689–714.
[12] Dai P, Chen Z, Chen S, Ju Y. Numerical experiments on reaction front propagation in n -heptane / air mixture with temperature gradient. Proc Combust Inst 2015;35:3045–52.
[13] Dai P, Chen Z. Supersonic reaction front propagation initiated by a hot spot in n -heptane / air mixture with multistage ignition. Combust Flame 2015;162:4183–93.
[14] Dai P, Qi C, Chen Z. Effects of initial temperature on autoignition and detonation development in dimethyl ether / air mixtures with temperature gradient. Proc Combust Inst 2018;36:3643–50.
[15] Dai P, Chen Z, Gan X. Autoignition and detonation development induced by a hot spot in fuel-lean and CO 2 diluted n-heptane / air mixtures. Combust Flame 2019;201:208–14.
[16] Yu H, Chen Z. End-gas autoignition and detonation development in a closed chamber. Combust Flame 2015;162:4102–11.
[17] Pan J, Wei H, Shu G, Chen R. Effect of pressure wave disturbance on auto-ignition mode transition and knocking intensity under enclosed conditions. Combust Flame 2017;185:63–74.
[18] Pan J, Shu G, Zhao P, Wei H, Chen Z. Interactions of flame propagation, auto-ignition and pressure wave during knocking combustion. Combust Flame 2016;164:319–28.
[19] Wei H, Chen C, Shu G, Liang X, Zhou L. Pressure wave evolution during two hot-spots autoignition within end-gas region under internal combustion engine-relevant conditions. Combust Flame 2018;189:142–54.
[20] Pan J, Wei H, Shu G, Pan M, Feng D, Li N. LES analysis for auto-ignition induced abnormal combustion based on a downsized SI engine. Appl Energy 2017;191:183–92.
[21] Pal P, Valorani M, Arias PG, Im HG, Wooldridge MS, Ciottoli PP, et al. Computational characterization of ignition regimes in a syngas/air mixture with temperature fluctuations. Proc Combust Inst 2016;36:3705–16.
[22] Luong MB, Yu GH, Lu T, Chung SH, Yoo CS. Direct numerical simulations of ignition of a lean n-heptane/air mixture with temperature and composition inhomogeneities relevant to HCCI and SCCI combustion. Combust Flame 2015;162:4566–85.
[23] Yoo CS, Lu T, Law CK. Direct numerical simulations of ignition of a lean n- heptane / air mixture with temperature inhomogeneities at constant volume: parametric study. Combust Flame 2011;158:1727–41.
[24] Chen JH, Hawkes ER, Sankaran R, Mason SD, Im HG. Direct numerical simulation of ignition front propagation in a constant volume with temperature inhomogeneities I. Fundamental analysis and diagnostics. Combust Flame 2006;145:128–44.
[25] Wei H, Gao D, Zhou L, Feng D, Chen R. Different combustion modes caused by flame-shock interactions in a confine d chamb er with a perforate d plate. Combust Flame 2017;178:277–85.
[26] Terashima H, Koshi M. Mechanisms of strong pressure wave generation in end-gas autoignition during knocking combustion. Combust Flame 2015;162:1944–56.
[27] Terashima H, Matsugi A, Koshi M. Origin and reactivity of hot-spots in end-gas autoignition with effects of negative temperature coefficients: relevance to pressure wave developments. Combust Flame 2017;184:324–34.
[28] Terashima H, Matsugi A, Koshi M. End-gas autoignition behaviors under pressure wave disturbance. Combust Flame 2019;203:204–16.
[29] Thomas GO, Edwards MJ, Edwards DH. Studies of detonation quenching by water sprays. Combust Sci Technol 1990;71:233–45.
[30] Smirnov NN, Nikitin VF, Khadem J, Alyari-shourekhdeli S. Onset of detonation in polydispersed fuel – air mixtures. Proc Combust Inst 2007;31:2195–204.
[31] Cheikhravat H, Goulier J, Bentaib A, Meynet N, Chaumeix N, Paillard CE. Effects of water sprays on flame propagation in hydrogen/air/steam mixtures. Proc Combust Inst 2015;35:2715–22.
[32] Niedzielska U, Kapusta LJ, Savard B, Teodorczyk A. Influence of water droplets on propagating detonations. J Loss Prev Process Ind 2017;50:229–36.
[33] Eidelman S, Burcatf A. Evolution of a detonation wave in a cloud of fuel droplets: part I. Influence of igniting explosion. AIAA J 1980;18:1103–9.
[34] Burcat A, Eidelmanf S. Evolution of a detonation wave in a cloud of fuel droplets: part II. Influence of fuel droplets. AIAA J 1980;18:1233–6.
[35] Yeom G, Chang K. Dissipation of shock wave in a gas-droplet mixture by droplet fragmentation. Int J Heat Mass Transf 2012;55:941–57.
[36] Schwer DA, Kailasanath K. Numerical simulations of the mitigation of unconfined explosions using water-mist. Proc Combust Inst 2007;31:2361–9.
[37] Watanabe H, Matsuo A, Matsuoka K. Numerical investigation on propagation behavior of gaseous detonation in water spray. Proc Combust Inst 2019;37:3617–26.
[38] Song Y, Zhang Q. Quantitative research on gas explosion inhibition by water mist. J Hazard Mater 2019;363:16–25.
[39] Boeck LR, Kink A, Oezdin D, Hasslberger J, Sattelmayer T. Influence of water mist on flame acceleration, DDT and detonation in H 2 -air mixtures. Int J Hydrogen Energy 2015;1–10.
[40] Aggarwal SK. A review of spray ignition phenomena: present status and future research. Prog Energy Combust Sci 1998;24:565–600.
[41] Bouali Z, Pera C, Reveillon J. Numerical analysis of the influence of two-phase flow mass and heat transfer on n-heptane autoignition. Combust Flame 2012;159:2056–68.
[42] Wang Z, Liu H, Reitz RD. Knocking combustion in spark-ignition engines. Prog Energy Combust Sci 2017;61:78–112.
[43] Harrington JA. Water addition to gasoline- effect on combustion, emissions, performance, and knock. SAE Int. Congr Expo; 1982.
[44] Hoppe F, Thewes M, Baumgarten H. Water injection for gasoline engines: potentials, challenges, and solutions. Int J Engine Res 2015;17:86–96.

[45] Chen Z, Burke MP, Ju Y. Effects of Lewis number and ignition energy on the determination of laminar flame speed using propagating spherical flames. Proc Combust Inst 2009;32(I):1253–60.
[46] Chen Z. Effects of radiation and compression on propagating spherical flames of methane/air mixtures near the lean flammability limit. Combust Flame 2010;157:2267–76.
[47] J.A.M. Kee RJ, Rupley FM. Report SAND89-8009B, 1989.
[48] Blouquin R, Joulin G. On the quenching of premixed flames by water sprays: influences of radiation and polydispersity. Symp Combust 1998;27:2829–37.
[49] Han W, Chen Z. Effects of finite-rate droplet evaporation on the ignition and propagation of premixed spherical spray flame. Combust Flame 2015;162:2128–39.
[50] Belyakov NS, Babushok VI, Minaev SS. Influence of water mist on propagation and suppression of laminar premixed flame. Combust Theory Model 2018;22:394–409.
[51] Abramzon B, Sirignano WA. Droplet vaporization model for spray combustion calculations. Int J Heat Mass Transf 1989;32:1605–18.
[52] Greenberg JB, Silverman I, Tambour Y. A new heterogeneous burning velocity formula for the propagation of a laminar flame front through a polydisperse spray of droplets. Combust Flame 1996;104:358–68.
[53] Greenberg JB. Finite-rate evaporation and droplet drag effects in spherical flame front propagation through a liquid fuel mist. Combust Flame 2007;148:187–97.
[54] Aggarwal SK, Sirignano WA. Numerical modeling of one-dimensional enclosed homogeneous and heterogeneous deflagrations. Comput Fluids 1984;12:145–58.
[55] Qiao L. Transient flame propagation process and flame-speed oscillation phenomenon in a carbon dust cloud. Combust Flame 2012;159:673–85.
[56] Ranz JWE, Marshall WR. Vaporation from drops, part I. Chem Eng Prog 1952;48:141–6.
[57] Ranz JWE, Marshall WR. Evaporation from drops, part I and part II. Chem Eng Prog 1952;48:173–80.
[58] Schiller L, Naumann A. A drag coefficient correlation. Zeitschrift Des Vereins Dtsch. Ingenieure 1935;77:318–20.
[59] Sazhin SS. Advanced models of fuel droplet heating and evaporation. Prog Energy Combust Sci 2006;32:162–214.
[60] Strang G. On the construction and comparison of difference schemes. SIAM J Numer Anal 2013;5:506–17.
[61] Brown PN, Byrne GD, Hindmarsh AC. VODE: a variable-coefficient ODE solver. SIAM J Sci Stat Comput 1989;10:1038–51.
[62] Sun M, Takayama K. Conservative smoothing on an adaptive quadrilateral grid. J Comput Phys 1999;150:143–80.
[63] Liu S, Hewson JC, Chen JH, Pitsch H. Effects of strain rate on high-pressure nonpremixed n -heptane autoignition in counterflow. Combust Flame 2004;137:320–39.